

Raman Imaging Spectroscopy of a Putative Microfossil from the ~3.46 Ga Apex Chert: Insights from Quartz Grain Orientation

D.M. Bower,¹ A. Steele,¹ M.D. Fries,² O.R. Green,³ and J.F. Lindsay^{4,*}

Abstract

The utility of nondestructive laser Raman for testing the biogenicity of microfossil-like structures in ancient rocks is promising, yet results from deposits like the ~3.46 Ga Apex chert remain contentious. The essence of the debate is that associated microstructures, which are not purported to be microfossils, also contain reduced carbon that displays Raman D- and G-band peaks similar to those seen in the purported microfossils. This has led to the hypothesis that all features including reported microfossils are due to compression of nonfossil carbon during crystal growth around quartz spherulites or more angular crystals. In this scenario, the precursor to this macromolecular carbon may or may not have been of biogenic origin, while the arcuate and linear features described would be pseudofossils. To test this hypothesis, we have undertaken 2-D micro-Raman imaging of the *Eoleptonema apex* holotype and associated features using instrumentation with a high spatial and spectral resolution. In addition to this, we utilized the ratio of two Raman active quartz mode intensities (I_{129}/I_{461}) to assess quartz grain orientation and grain-splitting artifacts. These data lead us to conclude that the holotype of *Eoleptonema apex* is a sheet-shaped pseudofossil that appears to be a carbon infilled intragranular crack; therefore other holotypes should be carefully reexamined for syngenicity. Key Words: Micro-Raman spectroscopy—Microfossils—Life detection—Archean—Apex chert. *Astrobiology* 16, 169–180.

1. Introduction

RAMAN SPECTROSCOPY has been used extensively in attempts to elucidate the biological nature and affinities of putative Archean microfossils (Kudryavstev *et al.*, 2001; Pasteris and Wopenka, 2003; Allwood *et al.*, 2006; Javaux *et al.*, 2010; Bower, 2011; Bower *et al.*, 2013), including those from the 3.46 Ga Apex chert assemblage (Brasier *et al.*, 2002, 2005; Schopf *et al.*, 2002a, 2002b, 2005; Schopf and Kudryavstev, 2009; Marshall *et al.*, 2011; Marshall *et al.*, 2012). Such pioneering studies have used confocal Raman peak mapping from a range of samples to attempt to deconvolve the ordered and disordered (D and G bands, respectively) peaks of macromolecular carbon as a signature of a biogenic for features identified as fossils by light microscopy techniques (Kudryavstev *et al.*, 2001; Schopf *et al.*, 2002a, 2005). Outside of recent studies examining the influence of hematite spectra (at 1313 cm^{-1}) on the misidentification of

carbon D-band peaks, most studies have only presented a restricted spectral range from parts of the purported microfossils (*e.g.*, Schopf *et al.*, 2002a, 2002b; Marshall *et al.*, 2011).

While several attempts have been made to investigate D- and G-band parameters such as peak positions, widths, and shoulders as a means of understanding the nature of the reduced carbon in ancient rocks, no single study has convincingly unearthed a series of useful parameters to absolutely determine biogenicity using this approach (Pasteris and Wopenka, 2003; Schopf and Kudryavstev, 2009; Marshall *et al.*, 2010; Bower *et al.*, 2013). Furthermore, the determination of biogenicity when using D- and G-band carbon is neither indicative of the primary origin nor the age of a given microfossil-like structure. Here, we assess the potential of a new and possibly less subjective method for testing the syngenicity of fossils within chert using quartz grain orientation combined with carbon D- and G-band parameters. We apply the technique to the analysis of

¹Geophysical Laboratory, Carnegie Institution of Washington, Washington, DC, USA.

²NASA Astromaterials Research and Exploration Science, Johnson Space Center, Houston, Texas, USA.

³Department of Earth Sciences, University of Oxford, Oxford, UK.

⁴Lunar and Planetary Science Institute, Houston, Texas, USA; *Deceased.

Eoleptonema apex and directly associated features within NHM slide V63729 from the Apex chert. This single filament was described as the holotype of a putatively beigiatoan bacterial microfossil (Schopf, 1993, Fig. 3F; Brasier *et al.*, 2002, 2005, object 29B1). It was one of 11 holotypes described from the ~ 3.46 Ga Apex chert (Schopf, 1993) and has been the subject of previous Raman peak imaging (Schopf *et al.*, 2002a). This study has gone much further than previous studies of *E. apex*, however, by analyzing a series of quartz standards, and using publicly available data from the RRUFF project, of differing crystal or laser orientations to further elucidate the context of fossils in chert. We then tested this method on Apex chert samples in parallel with polarized light microscopy to prove its validity at measuring quartz crystal orientation (Figs. 1 and 2). Assessing the crystal orientations of quartz within the Apex chert microfossil samples would then provide a test for syngenicity of this microfossil-like structure within its host rock.

Quartz exhibits trigonal symmetry of the space group $P3_121, P3_221$ and prominent Raman-active modes at 129, 201, and 461 cm^{-1} for 532 nm wavelength excitation laser (Scott and Porto, 1967; Fries and Claus, 1973; Bower and Steele, 2009; Fries and Steele, 2011). The intensity of the 129 cm^{-1} peak varies with the crystalline orientation of the quartz grains to the Raman excitation laser, while the intensity of the 461 cm^{-1} peak does not (Figs. 1 and 2). This subtle, but important, variation in intensity enables direct imaging of the size and orientation of quartz grains within a sample.

2. Materials and Methods

Analysis was conducted on a range of samples that included Apex chert samples V63165 and V63729 of the British Natural History Museum (NHM) (Schopf, 1993) and a thin-section sample of Apex chert provided by Martin Brasier. Analyses of quartz crystal standards of known

crystal orientation were performed on a collection of mineral standards prepared by Friederich von Heune. These standards were mounted as thin sections after X-ray diffraction confirmation of crystal orientation of 0, 10, 20, 45, 60, and 90 degrees relative to the crystalline c axis of quartz. Raman spectra were collected from these samples by using the same instrument and instrumental parameters used in analysis of the Apex samples. Furthermore, we downloaded and analyzed quartz spectra from the RRUFF project as an independent source of Raman spectra. For RRUFF spectral analyses, the Raman laser beam was oriented at 0, 45, and 90 degrees to a fiducial mark indicating the c axis of quartz (RRUFF files R040031-3, R050125-4, and R060604-3) (Downs, 2006).

Raman spectra and images were collected from thin sections of microfossils, previously reported microfossils, microfossil matrix composition, areas of differing quartz crystal size distribution confirmed by visualization under cross-polar imaging, and areas of interest associated with potential microfossil structures. Each feature was also inspected by transmitted and reflected light microscopy for depth within the thin section (Steele *et al.*, 2012). Raman imaging was performed with a WITec α -scanning near-field optical microscope that has been customized to incorporate confocal Raman spectroscopy imaging. The excitation source was a frequency-doubled solid-state YAG laser (532 nm) operating between 0.01 and 5 mW output power as measured at the Raman excitation focal plane using an Edmund Scientific laser power meter. Total laser power was measured as the average of triplicate measurements for each 0.01 mm step on the laser power output control dial. The resulting data set is stored as a calibrated curve of laser output versus measured laser power at the instrument focus, with one curve stored and routinely recalibrated for each objective lens. Objective lenses that were used included a $20\times$ long working distance and a $100\times$ oil immersion lens,

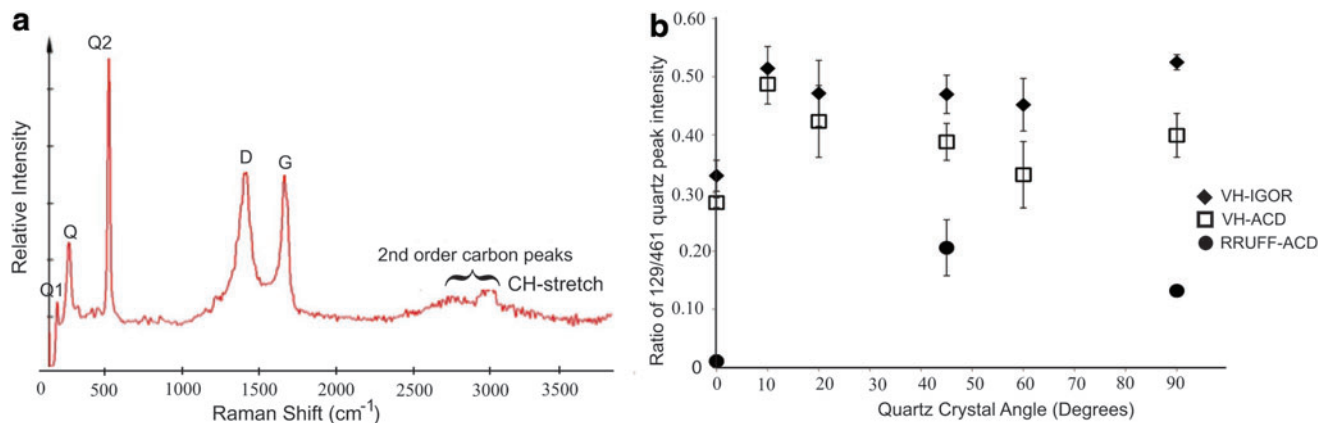


FIG. 1. (a) Average Raman spectra derived from over 8288 spectra from the feature (*E. apex*) shown in Fig. 2 (74 pixels per line; 112 lines). Q—quartz peaks at ~ 129 (Q1), 201 and 461 (Q2) cm^{-1} , respectively; D and G are the ordered and disordered carbon peaks at ~ 1350 and 1600 cm^{-1} , respectively. The second-order carbon bands representative of the CH stretch from the immersion oil are also labeled. (b) Comparative graph of the quartz $129/461\text{ cm}^{-1}$ intensity ratio using von Heune (VH) quartz thin-section data as processed through IGOR (VH-IGOR) and ACD/Labs (VH-ACD) and quartz standard data from the RRUFF database as processed through ACD/Labs (RRUFF-ACD). VH scans are relative to the crystalline c axis of quartz; each point is an average of 25 spectral acquisitions with triplicate measurements made at each crystalline orientation. RRUFF database (at 514 nm) used a separate method of peak intensity measurement at three angles of orientation. While the absolute ratios are not exactly the same, the trend lines show that there is an orientation dependence exhibited by the 129 cm^{-1} peak intensity.

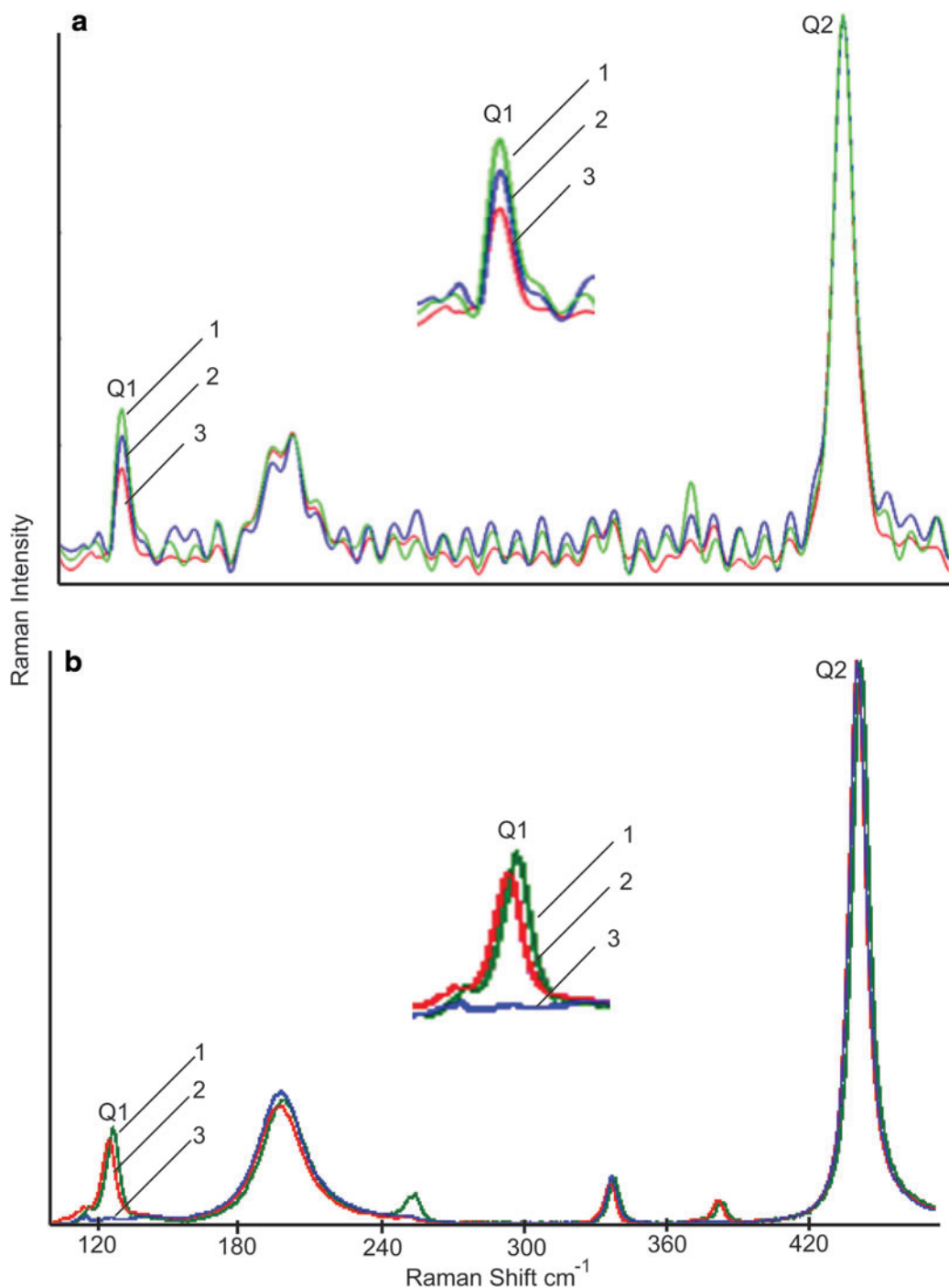


FIG. 2. Stack plots of quartz showing changing orientation of the crystal with reference to the c axis as exhibited by the variations in peak intensity of the 129 cm^{-1} (Q1) Raman E_g mode normalized to the 461 cm^{-1} (Q2) A_g mode. Each color represents one orientation; insets highlight three orientations and resulting variations in peak intensity of Q1. **(a)** Stack plot of quartz data as measured in this study; 1 = peak intensity perpendicular to the c axis, 2 = peak intensity 45° to the c axis, 3 = parallel to the c axis. **(b)** Stack plot of quartz data as measured by the RRUFF project; 1 = 45° to the c axis, 2 = perpendicular to the c axis, 3 = parallel to the c axis. (Color graphics available at www.liebertonline.com/ast)

with a $25\text{ }\mu\text{m}$ optical fiber acting as the confocal pinhole. The oil immersion lens was key to this analysis, as the refractive index of quartz and thickness of the sample made imaging of these microfossils almost impossible without it. Spectra were collected on a Peltier-cooled Marconi 40-11 CCD chip, after passing through a $f/4$ 300 mm focal length imaging spectrometer using a 600 lines/mm grating. The

lateral resolution of the instrument is as small as 270 nm when using the $100\times$ oil immersion objective, or 810 nm when using the $20\times$ objective. The depth of interaction during confocal analysis is $\sim 670\text{ nm}$ for transparent materials.

This instrument is capable of collecting either images or single spectra. Single-spectra mode allows the acquisition of a spectrum from a single spot on the target. Average spectra

are typically produced using integration times of 30 s per accumulation and 10 accumulations. Optical microscope images were captured by a camera system attached to the microscope. The height and width of the field of view were then measured and divided by the lateral resolution of the lens being used, to give the number of pixels per line. The instrument produces Raman images by accumulating a Raman spectrum at each image pixel as the sample stage translates. Raman peaks of interest were then chosen and their occurrence throughout the image computed by using a Gaussian fit to the data. After compilation, the image was checked for consistency in its peak mapping so as to ensure exclusion of similar peaks or increase in fluorescence background above the programmed background subtraction parameters. By selecting areas in which a particular peak occurred, average spectra were compiled from combining all the spectra from the pixels highlighted. This produces an average spectrum over the number of pixels chosen in the area of interest. For example, in the scan shown in Fig. 6 of *E. apex*, a scan area of $30 \times 20 \mu\text{m}$ was decided upon, and by using the $100\times$ oil immersion objective this enabled a resolution of 74×112 pixels per scan, yielding 8288 separate and spatially organized Raman spectra. WITec Project Plus software was used to map peaks of interest across the sample and compute peak ratio intensity maps of the D- and G-band carbon peaks (~ 1350 and 1610 cm^{-1} respectively), quartz peak intensities, and quartz crystal orientation by using the $129/461 \text{ cm}^{-1}$ peak intensity ratios.

Three-dimensional voxel renderings were created with optical images taken from map stacks at $1 \mu\text{m}$ intervals described by Brasier *et al.* (2002) using Olympus CellSens Dimension processing software.

Further data analysis was conducted on spectra generated in this project and from downloaded spectra from the RRUFF project database by using two different methods for background correction and peak intensity ratio calculation. In the first instance, data from the von Heune thin section analysis was exported as ASCII files into the Igor software package. Baseline correction was performed by using a spline fit function, and peaks were fit by using Gaussian profiles to produce peak intensity data; the results are displayed in Fig. 1b. Secondly, ACD/Labs Optical Workbench and CURVE packages were also used as a complementary technique to the first analysis. Spectra were imported as ASCII files; baseline correction was applied using midnoise, point-to-point editing, with each spectra being treated the same. Peak picking was then done manually before peak deconvolution was undertaken using a Gaussian-Lorentzian fit. The peak center and peak intensities of the quartz 129 and 461 cm^{-1} peaks were then recorded in a spreadsheet, after which the $129/461 \text{ cm}^{-1}$ peak ratios were calculated and plotted with Microsoft Excel. The purpose of expressing the 129 cm^{-1} mode as a ratio of $129/461 \text{ cm}^{-1}$ is to normalize all spectra against an invariant Raman peak intensity. The Raman mode at 461 cm^{-1} does not vary in intensity with quartz crystalline orientation as shown by Scott and Porto (1967), Fries and Claus (1973), and in Raman spectra available from the RRUFF database, which were collected independently from our laboratory. Furthermore, the 461 cm^{-1} peak varies only with changes in morphology and texture of the quartz samples and from defects in the sample such as surface scratches. The 129 cm^{-1} peak varies in intensity due to morphology, texture, defects, and quartz crystalline

orientation (Scott and Porto, 1967; Fries and Claus, 1973). Expressing the 129 cm^{-1} peak intensity as a $129/461 \text{ cm}^{-1}$ intensity ratio effectively removes the effects of texture, morphology, and any sample defects from the resulting data, which results in a value that only expresses the quartz crystallographic orientation. A twin-tailed paired *T* test using a 99.9% ($P=0.1$) confidence interval was applied to all data to test that the results obtained from any given quartz orientation are significantly different from other orientations.

3. Results

Figure 1a shows a spectrum averaged from all the pixels in a Raman image from *E. apex*, revealing quartz Raman peaks at 129 , 201 , and 461 cm^{-1} , the D and G bands of carbon at 1350 and 1610 cm^{-1} , respectively, as well as the second-order carbon peaks between 2700 and 2900 cm^{-1} , including a small -CH peak at 2850 cm^{-1} from the immersion oil used to image the features. Figure 1b shows the variance of the quartz 129 cm^{-1} Raman peak intensity, here normalized to the 461 cm^{-1} peak and expressed as $129/461 \text{ cm}^{-1}$ ratio, with respect to angle relative to the *c* axis on prepared thin sections of quartz having a known crystallographic orientation. This means that the intensity of the $129/461 \text{ cm}^{-1}$ peak ratio varies significantly between 0 and 90 degrees ($P=0.1$) with orientation in a repetitive pattern, so it is not possible to assign a definitive number to the angle of orientation of the crystals. Also shown in Fig. 1b are the results of applying a second deconvolution method to both the von Heune thin-section data generated in this study and the quartz spectra obtained from the RRUFF project. While the absolute ratios are not exactly the same between the two methods of deconvolution, the trend and statistical significance ($P=0.1$) of the results show that there is an orientation dependence on 129 cm^{-1} peak intensity. Furthermore, using stack plots of spectra from a commercial database in comparison to stack plots of our data removes any possible inference that the effect is due to instrument or data processing artifacts (Fig. 2).

By measuring the peak maxima of the 129 and 461 cm^{-1} peaks (I_{129} and I_{461} , respectively), calculating the ratio of the two, it is possible to use the WITec software to produce an image of the crystalline orientation of quartz grains in the polycrystalline matrix of the Apex samples. This is further emphasized in Fig. 3. Figure 3a shows an optical microscope image of the area to be scanned. In Fig. 3b, a spectral image of the quartz 461 cm^{-1} peak is mapped for that same area. Next, Fig. 3c shows a Raman spectral image of quartz I_{129}/I_{461} peak ratios that reveals the presence of multiple quartz grains of $3\text{--}5 \mu\text{m}$ in diameter. It is not possible to assign an absolute angle of these grains with respect to the *c* axis of quartz, but Fig. 3c shows that it is possible to produce an I_{129}/I_{461} peak ratio map that reveals the difference in crystal orientation of each crystal with respect to other crystals surrounding it. Producing a G-band carbon map (brighter areas represent higher peak intensity) shows the carbon present as arcuate structures that may be misinterpreted as possible fossils (Fig. 3d). Finally, a combined I_{129}/I_{461} and G-band image shows that the carbon is actually intergranular between quartz grains as opposed to being present as inclusions or enclosed microfossils, indicating that the carbon is contemporaneous with the quartz (Fig. 3e). This is also illustrated in Fig. 4 (a-b), where the boundary

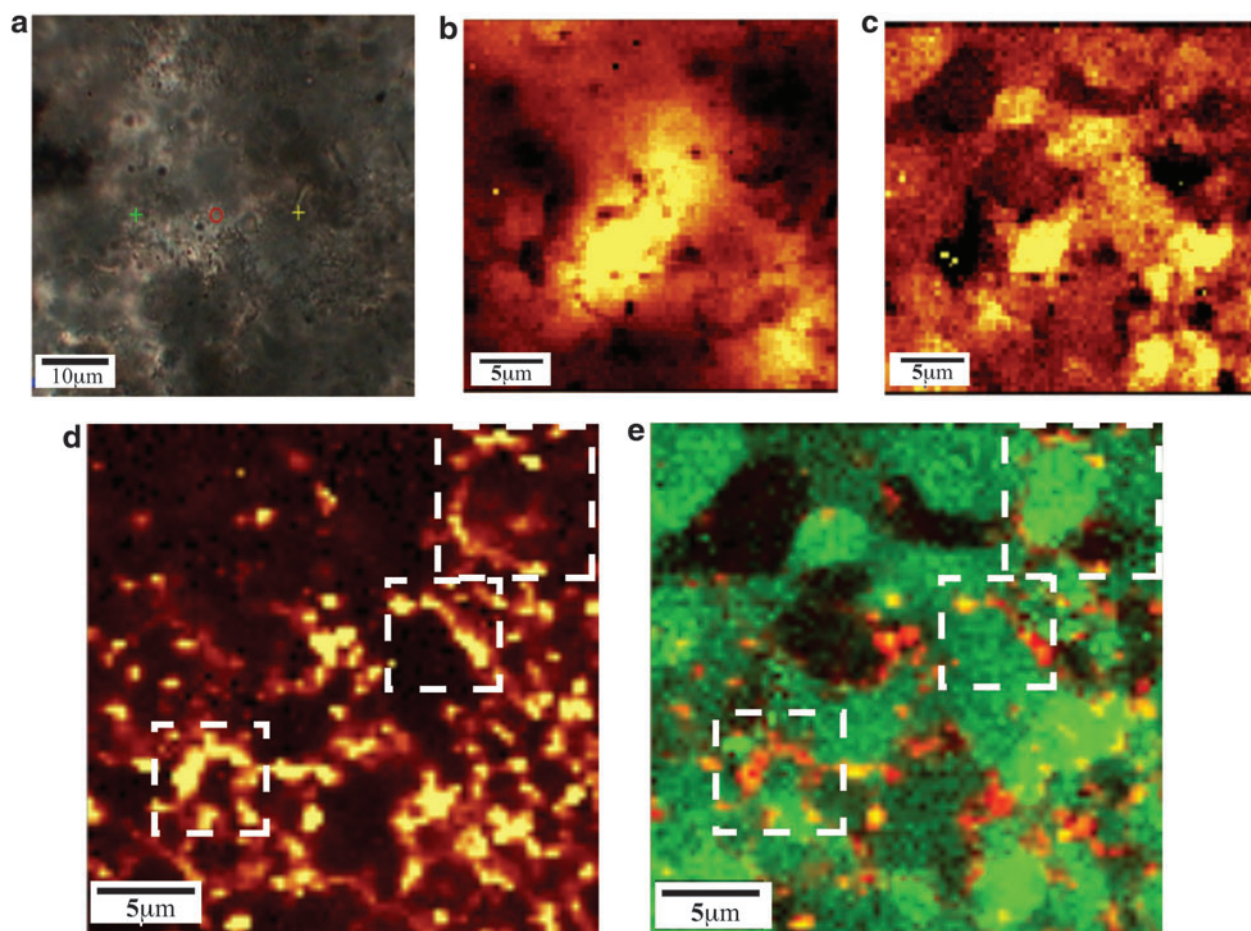


FIG. 3. Images showing the spatial relationships between quartz grains with G-band carbon. (a) Optical microscope image of scan area with typical matrix features found in the Apex samples. (b) The quartz 461 cm^{-1} peak intensity map; brighter areas show greater peak intensity. (c) Quartz I_{129}/I_{461} ratio image showing the presence of multiple quartz grains of $3\text{--}5\ \mu\text{m}$ in diameter. (d) Carbon G-band (1600 cm^{-1}) peak intensity map, where brighter areas indicate higher peak intensity. (e) Color montage of quartz, I_{129}/I_{461} (green) and G-band carbon (red); boxes highlight areas corresponding to (d) where carbon is wrapped around quartz grain boundaries. (Color graphics available at www.liebertonline.com/ast)

between two different generations of quartz is delineated by optical microscopy. An image produced when using the I_{129}/I_{461} peak ratios shows the difference between the two types of quartz even more clearly, with monocrystalline quartz on the left of the image and multiple grains $\sim 3\text{--}5\ \mu\text{m}$ in diameter on the right (Fig. 4c). Creating a quartz/carbon image reveals that the carbon (shown as brighter areas in the image) is detected interstitially only in the microcrystalline quartz (Fig. 4d). Further chemical imaging also revealed anatase and chamosite (also represented by brighter areas in images) associated with the carbon in the microcrystalline quartz but not in the monocrystalline quartz (Fig. 4e–4f, 4g–4j).

By focusing on a microcrystalline area of quartz, intergranular features are imaged with higher resolution (Fig. 5). For example, in the secondary Apex fabrics, a subrounded structure is detected and clearly imaged to obtain compositional details and its spatial relationship with the surrounding quartz (Fig. 5). The feature itself is $\sim 15\ \mu\text{m}$ in diameter and composed of a mixture of hematite and goethite, barite, macromolecular carbon, and anatase, a mineral assemblage often associated with hydrothermal deposits in this and related beds (Van Kranendonk and Pirajano, 2004; Pinti *et al.*, 2009). Maps of hematite 408 cm^{-1} peak (Fig. 5c)

and of the carbon G band (1600 cm^{-1}) plus hematite-goethite (Fig. 5d) are compared to show their coexistence. The I_{129}/I_{461} peak ratio map of the microcrystalline quartz displays a number of individual quartz grains that appear to terminate at, or grow away from, the subrounded feature (Fig. 5e, 5f). The composition and intragranular nature of the structure supports findings by Brasier *et al.* (2002, 2005) from the immediate vicinity of *E. apex*, in which rounded fragments within the fabrics of secondary fissure-filling hydrothermal origin contained carbonaceous matter accompanied by a similar mineral suite.

Using our methods on the entire $\sim 70\ \mu\text{m}$ long feature that contains the *E. apex* holotype reveals some interesting characteristics regarding the nature of the “fossil” (Figs. 6–8). Figure 6a shows the whole structure with what appears to be a balloonlike feature at one end as reported by Brasier *et al.* (2002). In Fig. 6b, the $\sim 4\ \mu\text{m}$ original portion of the *E. apex* fossil analyzed by Schopf *et al.* (2002a,b) is delineated, showing that this region only represents a small fraction of a much larger structure. Mapping of the intensity of the major quartz peak at $\sim 461\text{ cm}^{-1}$ (bright areas indicate high quartz peak intensity) shows a very homogeneous distribution of quartz, except for within and around the

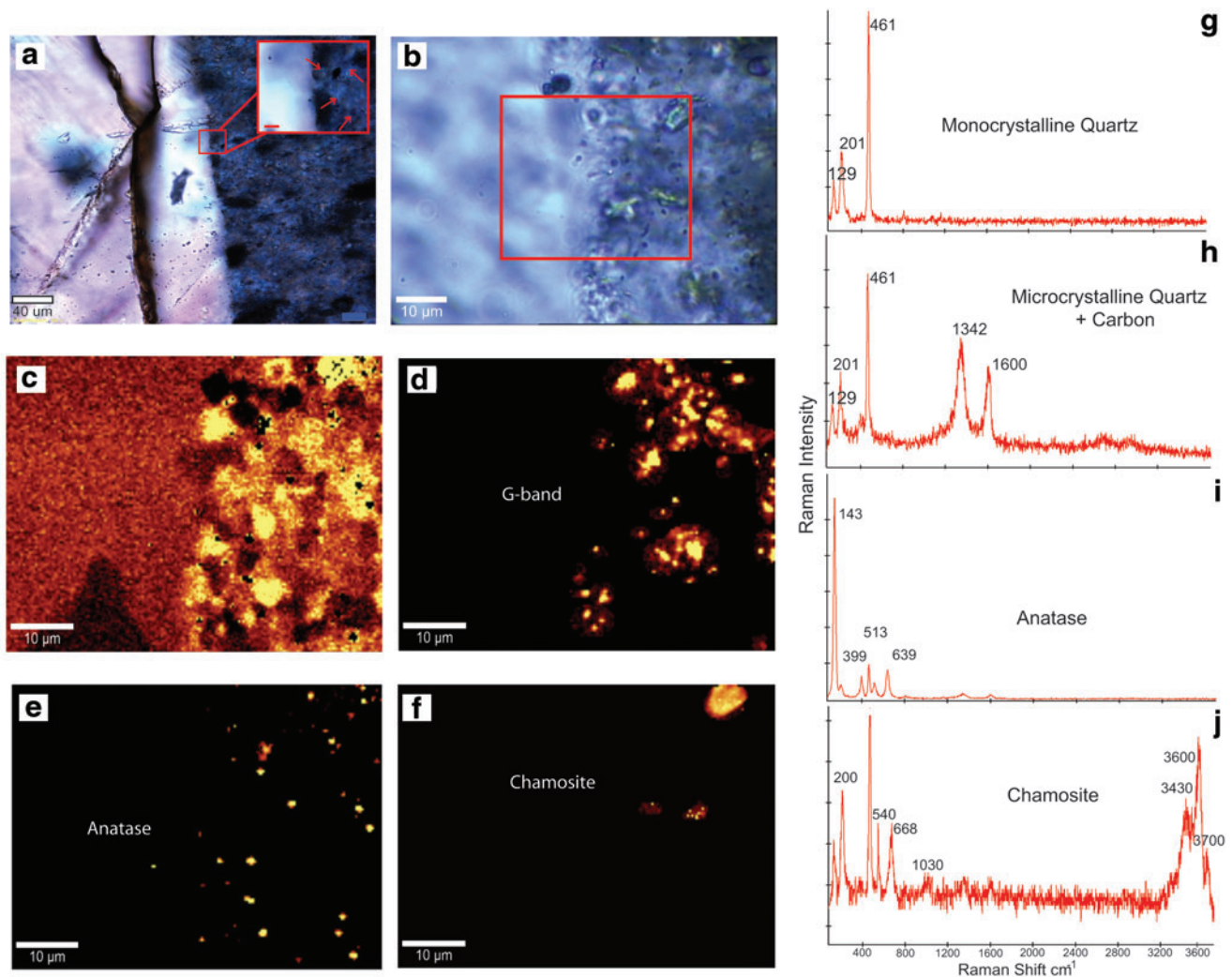


FIG. 4. Images showing the boundary between a large monocrystalline quartz grain and microcrystalline grains of quartz. (a) Cross-polarized image of scan area overview (at 40 \times); specific scan area indicated by box. Inset of boxed area zoomed in shows outlines of individual microcrystalline grains $\sim 3\text{--}5\ \mu\text{m}$ in diameter indicated by arrows. Scale bar within red box = $10\ \mu\text{m}$. (b) Plane-polarized image of location of specific scan area at higher magnification (100 \times) with clear delineation between two quartz types. (c) Quartz I_{129}/I_{461} ratio image clearly showing the edge between multiple quartz grains of $3\text{--}5\ \mu\text{m}$ in the microcrystalline quartz and the $>40\ \mu\text{m}$ grain of the monocrystalline quartz. Maps of (d) carbon, (e) anatase, and (f) chamosite peak intensities (indicated by brighter areas) reveal a specific association within the interstices of the microcrystalline quartz; none were detected in the monocrystalline quartz. (g) Spectra from monocrystalline quartz, main peaks of 129, 201, 461 cm^{-1} in contrast with (h) spectra from microcrystalline quartz, with main peaks of 129, 201, 394, and 461 cm^{-1} as well as the D-band (1342 cm^{-1}) and G-band (1600 cm^{-1}) carbon shown in (e). (i) Main spectral peaks for the anatase dispersed in the microcrystalline quartz at 143, 399, 513, 639 cm^{-1} . (j) Chamosite spectra showing strong diagnostic peaks at 200, 540, 668, 1030, 3430, 3600, and 3700 cm^{-1} . (Color graphics available at www.liebertonline.com/ast)

holotype, where the peak intensity is diminished (Fig. 6c). Carbon mapping reveals the secondary origin of this structure, with carbon in and around the feature (Fig. 6d, 6e). Most tellingly, when the carbon peak distribution (D and G band) is followed through this structure by using the methods of Schopf *et al.* (2005), the ratio of the G/D Raman peaks of macromolecular carbon reveals the presence of two very distinct populations, in which areas are either dominated by the disordered carbon band ($\sim 1350\ \text{cm}^{-1}$; Fig. 6e, blue/purple) or by the ordered or graphitic band of carbon ($\sim 1610\ \text{cm}^{-1}$; Fig. 6e, yellow/orange). Nor does the graphitic sheet appear to be a single coherent feature; rather, it ramifies into several distinct features along its left side.

Peak mapping of the ratio of the quartz I_{129}/I_{461} peaks shows a variation that is markedly different to that seen in the quartz 461 cm^{-1} intensity map (Fig. 6f). Intriguingly, quartz crystal orientation mapping in the matrix surrounding the *E. apex* holotype shows that the “fossil” actually transects individual quartz grains. To be sure that the quartz crystal orientation across the feature in Fig. 6f was not an artifact, measurements of the quartz peak intensity were extracted from individual spectra in areas selected from the transected grain fragments. These are labeled as grains A:B; C:D, E:F, and G:H. For example, the I_{129}/I_{461} peak maxima ratios are 0.140 ± 0.025 ($n=86$) for A, 0.151 ± 0.025 ($n=36$) for B, and 0.109 ± 0.056 ($n=7474$) for the entire image

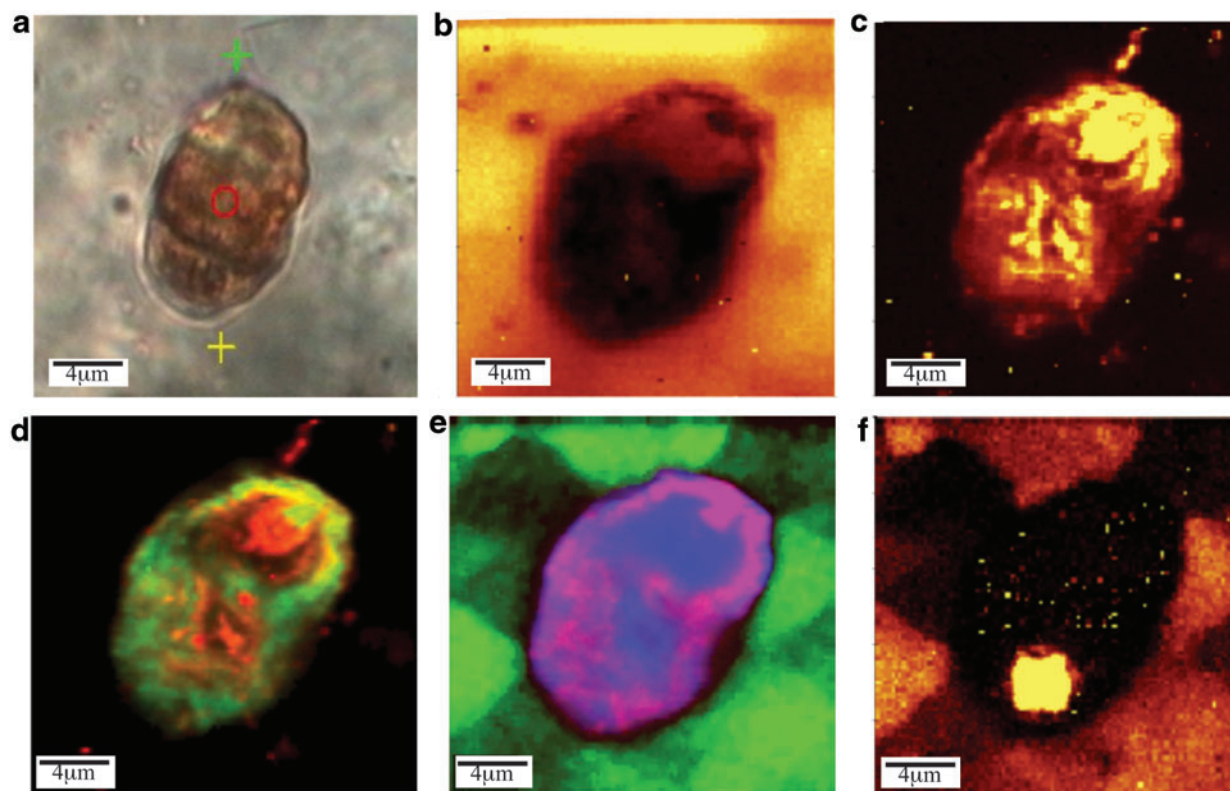


FIG. 5. Details of a subrounded feature found in the secondary fabric of the Apex chert. (a) Transmitted light microscope image showing the feature. (b) Quartz 461 cm^{-1} peak intensity map; bright areas indicate highest intensity. (c) Hematite 408 cm^{-1} peak intensity mapped; bright areas indicate highest intensity. (d) G-band 1600 cm^{-1} peak intensity (red) and mixed iron oxide, goethite 998 cm^{-1} , 3095 cm^{-1} /hematite 408 cm^{-1} , 613 cm^{-1} , 1313 cm^{-1} (green). (e) Quartz I_{129}/I_{461} peak ratio map (green) showing distinct intergranular relationship with subrounded feature composed of mixed iron oxide, goethite/hematite (red) and barite, 985 cm^{-1} peak center (blue). (f) Quartz I_{129}/I_{461} peak ratio map (red) and a $2\text{ }\mu\text{m}$ grain of anatase (yellow) also associated with this feature as indicated by peaks at $\sim 144\text{ cm}^{-1}$, 197 cm^{-1} , and 399 cm^{-1} . (Color graphics available at www.liebertonline.com/ast)

(based on the von Heune data collected in this study). This variation in I_{129}/I_{461} peak maxima ratios is clearly seen in stack plots of raw spectra (Fig. 6g). A T test comparison of these mean values produces $T=2.26$ for $T_{\text{crit}}=2.58$ ($P=0.01$, 120 degrees of freedom), proving the null hypothesis that the means of the two sets of values do not differ significantly and therefore the grain pairs across the crack from each other can be transected fragments that preserve their original (precrack) direction. The grain marked (a) appears to have resisted cracking, thus diverting the fracture and forming the 90° step seen midway through the feature. The most parsimonious explanation for this is that the purported *E. apex* structure is not a *bona fide* individual microfossil. It is part of an intragranular crack infilled by macromolecular carbon.

Profiling of the feature that contains *E. apex* reveals a width of $\sim 1.6\text{ }\mu\text{m}$ that is $\sim 3\text{ }\mu\text{m}$ deep in direct contact with a sheetlike feature (or crack) that is at least $22\text{ }\mu\text{m}$ long, giving it dimensions unlike any known individual organism (Fig. 7a–7c). Continued depth profiling at $1\text{ }\mu\text{m}$ intervals of the carbon peaks associated with the ballooning, sheetlike feature attached to its northern end shows that this carbon communicates with carbon in the quartz matrix as well as in cracks and fissures for $\sim 70\text{ }\mu\text{m}$ through the thin section (Fig. 7b–7d). Furthermore, blended image and isosurface 3-D voxel renderings (optical to voxel) of the complete feature

made from stacks of optical images show the “fossil’s” connection to fissure and matrix carbon (Fig. 8b–8d). As illustrated in an isosurface projection of the extensive carbonaceous areas, the features do not resemble anything biological, and carbon-filled fractures seem to be the only plausible explanation (Fig. 8d).

4. Discussion

Previous detailed studies of the petrology of the NHM samples have shown at least four generations of fissure-filling quartz (Brasier *et al.*, 2005). Of the 48 reported candidate microfossils, only 21 were found in first-generation fissure filling material or in clasts (Schopf, 1993; Brasier *et al.*, 2005). At least 60% of the reported microfossils, including *E. apex*, were found in secondary fabrics and not within clasts of any kind. Of those features found in secondary fabrics, at least 50% were found to be arcuate, which is consistent with formation around spherulites or crystals (Brasier *et al.*, 2005). The use of I_{129}/I_{461} peak ratio of quartz clearly demonstrated, both with data generated from this study and publicly accessible data, that this ratio can clearly image the crystal orientation of quartz in these samples (Figs. 3–7). The use of the quartz I_{129}/I_{461} peak ratio mapping relies on the quartz 129 cm^{-1} exhibiting a marked intensity dependence upon

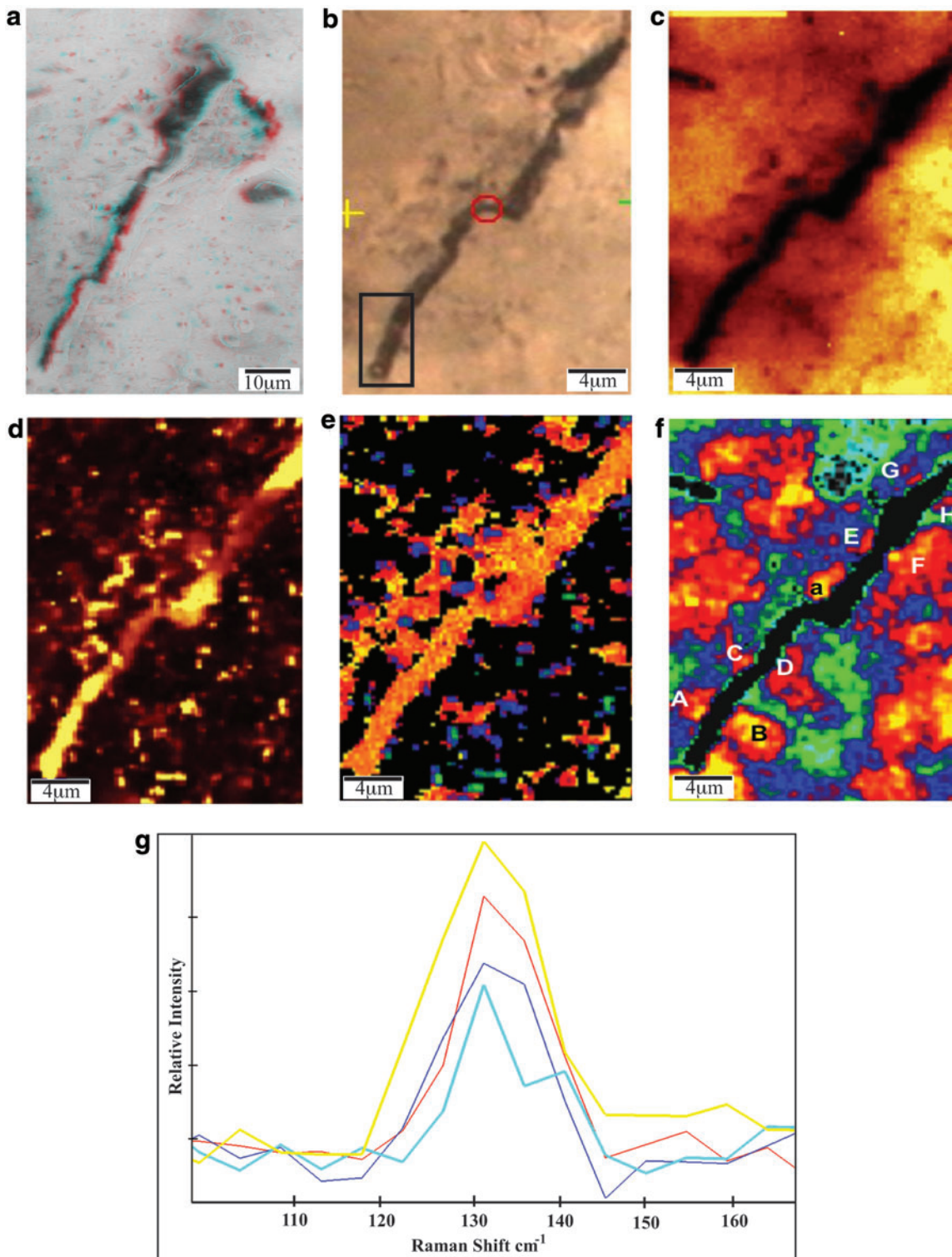


FIG. 6. Optical (a, b) and Raman peak mapping (c–f) photomicrographs of the putative microfossil—*E. apex* (holotype) from NHM slide V63729. (a) 3-D red-cyan anaglyph of the complete *E. apex* assemblage showing how the fossil connects with a balloonlike feature at one end. (b) Optical microscope image of the area of the feature included in the Raman spectral maps (c–f). Black box at lower end shows the area previously Raman peak-mapped (Schopf *et al.*, 2002a,b). (c) Raman spectral map of quartz 461 cm^{-1} peak intensity; brighter areas indicate higher peak intensity. (d) Spectral map of disordered carbon D band ($\sim 1350\text{ cm}^{-1}$), where brighter areas indicate higher peak intensity. (e) Spectral map of the G/D Raman peak ratio of macromolecular carbon showing two distinct populations [blue/purple areas that are dominated by the disordered carbon band ($\sim 1350\text{ cm}^{-1}$) and yellow/orange areas that are dominated by the ordered or graphitic band of carbon ($\sim 1600\text{ cm}^{-1}$)]. (f) Spectral map of quartz I_{129}/I_{461} intensity ratio showing quartz crystalline orientation relative to the Raman excitation beam. Low ratio values are blue; higher ratio values are yellow (0.16–0.26, respectively). Grains A:B, C:D, E:F, and G:H appear to be paired fragments across an intragranular crack. The grain marked “a” appears to have resisted cracking, thus diverting the fracture and forming the 90° step seen midway through the feature. (g) Four raw spectra taken from map in (f) where the colors of each spectrum (blue, green, red, yellow) are correlated to the color of the spectra in the figure normalized to the 461 cm^{-1} peak intensity; note the change in height of the 129 cm^{-1} peak. (Color graphics available at www.liebertonline.com/ast)

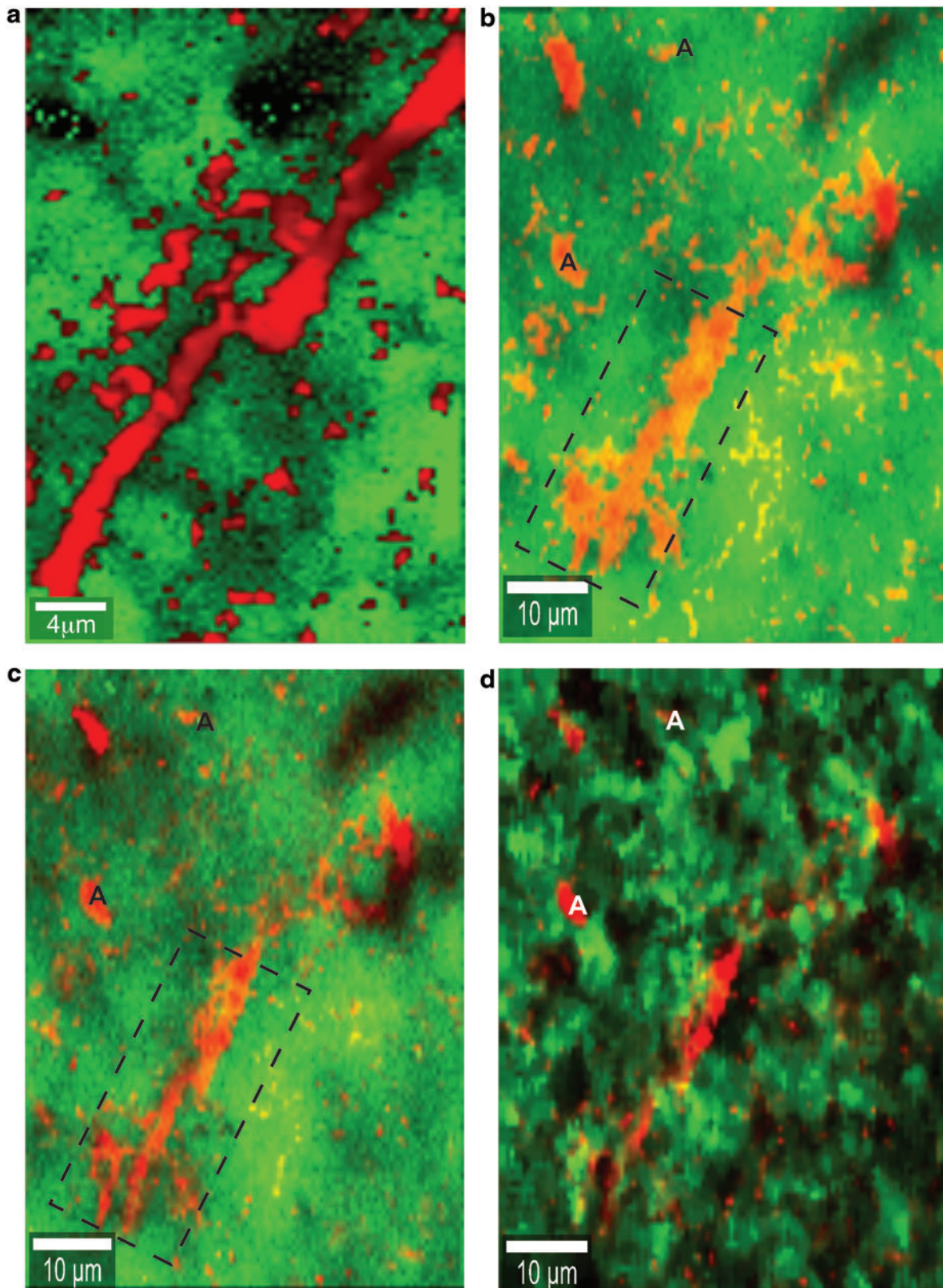


FIG. 7. Raman spectral maps of G-band carbon at three depth increments showing the *E. apex* feature communicates with carbon-filled cracks. (a) G-band map from main scan of *E. apex* used in this paper at 14.4 microns into the thin section at 100 \times . (b) G-band map of entire feature at 15.4 microns into the thin section at 20 \times showing a clear connection between the *E. apex* structure and the crack outside of the main scan area within the dashed box; some graphitic areas also contained anatase (A). (c) G-band map of entire feature at 16.4 microns in. Dotted box highlights main part of feature described in this paper; anatase is also labeled (A). (d) Quartz I_{129}/I_{461} map (green) combined with G-band carbon map (red) at 16.4 microns into the thin section, revealing the intergranular nature of much of the carbon. (Color graphics available at www.liebertonline.com/ast)

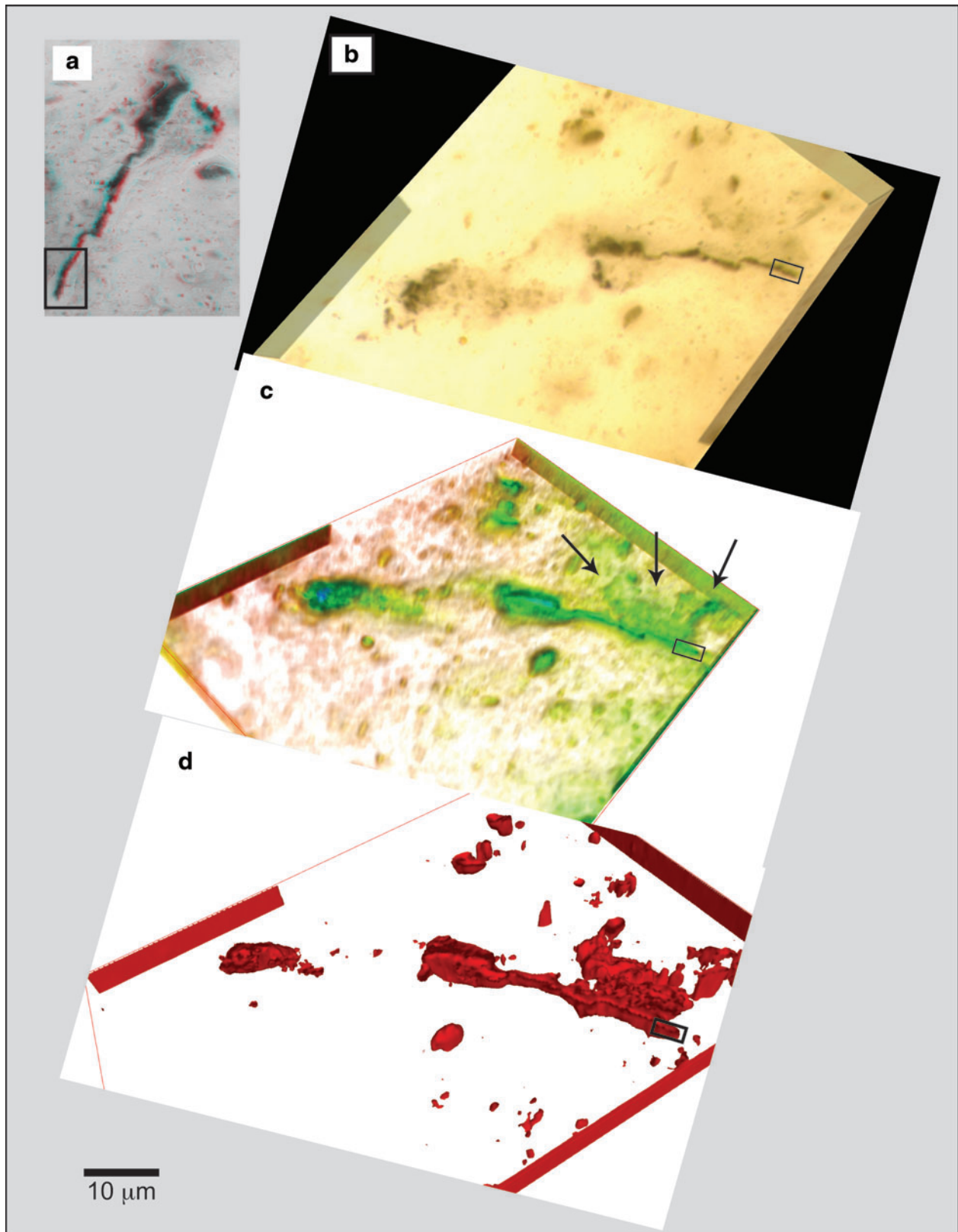


FIG. 8. Three-dimensional renderings of the entire feature that contains *E. apex*. (a) Image from Fig. 6 (this paper) showing isolated portion of feature used for Raman analysis in Schopf *et al.* (2002a,b) (in boxed area). (b) A 3-D montage view of the entire feature from optical imaging. (c) Blended optical and voxel rendering of optical images and arrows point to sheetlike area of carbon connected to the region that contains *E. apex*. (d) Isosurface projection of voxel-rendered images with subtracted background to reveal extensive cracklike feature and other carbon-rich areas associated with the *E. apex* feature. Boxes indicate original region analyzed by Raman in Schopf *et al.* (2002a,b).

excitation geometry (Scott and Porto, 1967). Normalized to the invariant Raman quartz mode at 461 cm^{-1} , it is not surprising that this I_{129}/I_{461} ratio reveals quartz crystal orientation (Fries and Claus, 1973). Our collected data alongside the use of publicly available data from the RRUFF database are all therefore consistent with the established literature on Raman peak assignments in quartz.

Recent studies have tried to nullify the debate on biogenicity of carbon by inferring that metrics obtained on the D band of carbon (1350 cm^{-1}) are flawed due to the possible presence of a resonance Raman peak of hematite (1310 cm^{-1}) in the samples. In this study, as we are obtaining spectra from 0 to 3800 cm^{-1} , only the G band of carbon is used to produce carbon maps (1600 cm^{-1}), and hematite is mapped using lower wavenumber bands (408 cm^{-1}). When the D band has been used, in the case of the analysis of D-to-G-band characteristics (Figs. 4 and 6), the peak center mapping conducted was centered at 1350 cm^{-1} and not 1310 cm^{-1} where the resonant band of hematite would interfere with the analysis. Furthermore, the spectra obtained at each pixel of the resultant D-band maps were checked for the presence of lower wavenumber peaks of hematite that could interfere with peak intensity statistics. It should also be noted that no hematite was detected in or along the edges of the *E. apex* feature; there were only carbon and occasional grains of anatase (Figs. 7 and 8). Therefore, the discussion of hematite interfering with the generated carbon maps is not applicable to this study (Marshall and Marshall, 2011, 2013; Marshall *et al.*, 2011).

Using D-to-G intensity ratios, we find at least two distinct populations of carbon in and around the holotype of *E. apex*, which is consistent with the secondary infilling of a crack. Lastly, our analyses of the entire feature show that *E. apex* is a small part of a larger nonbiological structure (Figs. 7 and 8), consistent with the observations of Brasier *et al.* (2002) and Brasier *et al.* (2004). We conclude, therefore, that the *E. apex* feature was formed by carbon infilling a fissure to form a sheet within the rock at some stage during deposition of a secondary hydrothermal fabric (Marshall *et al.*, 2014; Sforna *et al.*, 2014).

The micro-Raman imaging techniques highlighted in this study have helped clarify the mineralogical context for a reported ancient microfossil holotype. Using the combined techniques of quartz peak ratios and carbon mapping at incremental depths, we clearly see that at least one of the purported cell-like structures as described by Schopf (1993) is best interpreted as a secondary mineralogical feature. Given the assertions of biogenicity from previous Raman analysis of the carbon in this fossil, comparable techniques now need to be applied to other early Archean fossils to provide a comprehensive screen of the mineralogical context for their genesis and purported biogenicity (Schopf and Kudryavstev, 2012; Pinti *et al.*, 2013). The techniques highlighted in this manuscript provide a new and effective way to allow accurate determination of the syngenetic of any candidate microfossil within its rock matrix, which is a primary criterion for establishing whether a reported fossil is truly ancient (Buick, 1990; Brasier *et al.*, 2004; Schopf, 2004; Lindsay *et al.*, 2005; Javaux and Benzerara, 2009).

5. Conclusions

Raman imaging of quartz crystalline orientation is a powerful new tool in the investigation of quartz-hosted,

purported microfossils. In the examples shown here, our findings question conclusions that arise from previous, but limited, Raman microspectrometric studies indicating that the microfossil-like structure called *E. apex* is truly a 3.46 Ga filamentous organism (Schopf *et al.*, 2002a, 2002b). We argue that this feature can be more parsimoniously explained as the result of a secondary process involving silica fracturing during crystal growth from a silica carbon-rich fluid. No conclusions can yet be made with regard to a biogenic source for this carbon infilling, but this analysis has shown that at least two generations of carbon are present in the Apex chert. It remains possible that the source of this carbon resulted from remobilization of $<1\text{ }\mu\text{m}$ cellular remains and products trapped at some indeterminable time after formation of the secondary hydrothermal silica in which *E. apex* is now embedded (Buick, 1984; De Gregorio and Sharp, 2006). However, there remains the possibility that this carbon was generated abiotically during hydrothermal processes (Lindsay *et al.*, 2005; De Gregorio and Sharp, 2006). Until the crystallographic context and carbon content of each Apex chert microfossil have been thoroughly analyzed, these structures should be regarded as pseudofossils.

Acknowledgments

We would like to acknowledge the support of NASA SRLIDA and ASTEP (A. Steele, PI), Natural History Museum London for loan of the thin sections, WITec GmbH, NAI Postdoctoral Program, and Oak Ridge Associated Universities. We thank Martin Brasier, Maia Schweizer, and David Wacey for useful comments on the manuscript. A special thanks to E. Leporida for reminding us the truth is what matters most. This paper is dedicated to the memory of John Lindsay and Martin D. Brasier.

References

- Allwood, A.C., Walter, M.R., and Marshall, C.P. (2006) Raman spectroscopy reveals thermal palaeoenvironments of c. 3.5 billion-year-old organic matter. *Vib Spectrosc* 41:190–197.
- Bower, D.M. (2011) Micro-Raman spectroscopic investigations of mineral assemblages in parallel to bedding laminae in 2.9 Ga sandstones of the Pongola Supergroup, South Africa. *J Raman Spectrosc* 42:1626–1633.
- Bower, D.M. and Steele, A. (2009) Investigations of the nature and provenance of mineral and carbonaceous material in fossiliferous cherts: revisiting the 1.9 Ga Gunflint Formation. In *Geological Society of America Abstracts with Programs*, Vol. 41, Geological Society of America, Boulder, CO, p 45.
- Bower, D.M., Steele, A., Fries, M.D., and Kater, L. (2013) Micro-Raman spectroscopy of carbonaceous material in microfossils and meteorites: improving a method for life detection. *Astrobiology* 13:103–113.
- Brasier, M.D., Green, O.R., Jephcoat, A.P., Kleppe, A.K., Van Kranendonk, M.J., Lindsay, J.F., Steele, A., and Grassineau, N.V. (2002) Questioning the evidence for Earth's oldest fossils. *Nature* 416:76–81.
- Brasier, M.D., Green, O.R., Lindsay, J.F., and Steele, A. (2004) Earth's oldest (~ 3.5 Ga) fossils and the 'Early Eden hypothesis': questioning the evidence. *Orig Life Evol Biosph* 34:257–269.
- Brasier, M.D., Green, O.R., Lindsay, J.F., McLoughlin, N., Steele, A., and Stoakes, C. (2005) Critical testing of Earth's oldest putative fossil assemblage from the ~ 3.5 Ga Apex

- chert, Chinaman Creek, Western Australia. *Precambrian Res* 140:55–102.
- Buick, R. (1984) Carbonaceous filaments from the North Pole, Western Australia: are they fossil bacteria in Archean stromatolites? *Precambrian Res* 24:157–172.
- Buick, R. (1990) Microfossil recognition in Archean rocks: an appraisal of spheroids and filaments from a 3500 M.Y. old chert-barite unit at North Pole, Western Australia. *Palaios* 5:441–459.
- De Gregorio, B.T. and Sharp, T.G. (2006) The structure and distribution of carbon in 3.5 Ga Apex chert: implications for the biogenicity of Earth's oldest putative microfossils. *Am Mineral* 91:784–789.
- Downs, R.T. (2006) The RRUFF project: an integrated study of the chemistry, crystallography, Raman and infrared spectroscopy of minerals [abstract 003-13]. In *Program and Abstracts of the 19th General Meeting of the International Mineralogical Association*, Kobe, Japan.
- Fries, J. and Claus, R. (1973) Phonon and polarization spectra of B-quartz. *J Raman Spectrosc* 1:71–81.
- Fries, M.D. and Steele, A. (2011) Raman spectroscopy and confocal Raman imaging in mineralogy and petrography. In *Confocal Raman Microscopy*, edited by T. Dieing, O. Hollricher, and J. Toporskis, Springer-Verlag, Berlin, pp 111–136.
- Javaux, E.J. and Benzerara, K. (2009) Microfossils. *C R Palevol* 8:605–615.
- Javaux, E.J., Marshall, C.P., and Bekker, A. (2010) Organic-walled microfossils in 3.2-billion-year-old shallow-marine siliciclastic deposits. *Nature* 463:934–938.
- Kudryavstev, A.B., Schopf, J.W., Agresti, D.G., and Wdowiak, T.J. (2001) *In situ* laser-Raman imagery of Precambrian microscopic fossils. *Proc Natl Acad Sci USA* 98:823–826.
- Lindsay, J.F., Brasier, M.D., McLoughlin, N., Green, O.R., Fogel, M.L., Steele, A., and Mertzman, S.A. (2005) The problem of deep carbon—an Archean paradox. *Precambrian Res* 143:1–22.
- Marshall, A.O., Emry, J.R., and Marshall, C.P. (2012) Multiple generations of carbon in the Apex chert and implications for preservation of microfossils. *Astrobiology* 12:160–166.
- Marshall, A.O., Jehlicka, J., Rouzaud, J.N., and Marshall, C.P. (2014) Multiple generations of carbonaceous material deposited in Apex chert by basin-scale pervasive hydrothermal flow. *Gondwana Research* 25:284–289.
- Marshall, C.P. and Marshall, A.O. (2011) Hematite and carbonaceous materials in geological samples: a cautionary tale. *Spectrochim Acta A Mol Biomol Spectrosc* 80:133–137.
- Marshall, C.P. and Marshall, A.O. (2013) Raman hyperspectral imaging of microfossils: potential pitfalls. *Astrobiology* 13: 920–921.
- Marshall, C.P., Edwards, H.G.M., and Jehlicka, J. (2010) Understanding the application of Raman spectroscopy to the detection of traces of life. *Astrobiology* 10:229–243.
- Marshall, C.P., Emry, J.R., and Marshall, A.O. (2011) Hematite pseudomicrofossils present in the 3.5-billion-year-old Apex Chert. *Nat Geosci* 4:240–243.
- Pasteris, J.D. and Wopenka, B. (2003) Necessary, but not sufficient: Raman identification of disordered carbon as a signature of ancient life. *Astrobiology* 3:727–738.
- Pinti, D.L., Mineau, R., and Clement, V. (2009) Hydrothermal alteration and microfossil artefacts of the 3,465-million-year-old Apex chert. *Nat Geosci* 2:640–643.
- Pinti, D.L., Mineau, R., and Clement, V. (2013) Comment on “Biogenicity of Earth's earliest fossils: a resolution of the controversy” by J. William Schopf and Anatoliy Kudryavstev, *Gondwana Research* 22 (2012), 761–771. *Gondwana Research* 23:1652–1653.
- Schopf, J.W. (1993) Microfossils of the Early Archean Apex chert: new evidence of the antiquity of life. *Science* 260:640–646.
- Schopf, J.W. (2004) Earth's earliest biosphere: status of the hunt. In *The Precambrian Earth: Tempos and Events*, edited by P.G. Eriksson, W. Altermann, D.R. Nelson, W.U. Mueller, and O. Catuneanus, Elsevier, Amsterdam, pp 516–539.
- Schopf, J.W. and Kudryavstev, A.B. (2009) Confocal laser scanning microscopy and Raman imagery of ancient microscopic fossils. *Precambrian Res* 173:39–49.
- Schopf, J.W. and Kudryavstev, A.B. (2012) Biogenicity of Earth's earliest fossils: a resolution of the controversy. *Gondwana Research* 22:761–771.
- Schopf, J.W., Kudryavstev, A.B., Agresti, D.G., Wdowiak, T.J., and Czaja, A.D. (2002a) Laser-Raman imagery of Earth's earliest fossils. *Nature* 416:73–76.
- Schopf, J.W., Kudryavstev, A.B., Agresti, D.G., Wdowiak, T.J., and Czaja, A.D. (2002b) Images of Earth's earliest fossils? (discussion and reply). *Nature* 420:476–477.
- Schopf, J.W., Kudryavstev, A.B., Agresti, D.G., Czaja, A.D., and Wdowiak, T.J. (2005) Raman imagery: a new approach to assess the geochemical maturity and biogenicity of permineralized Precambrian fossils. *Astrobiology* 5:333–371.
- Scott, J.F. and Porto, S.P.S. (1967) Longitudinal and transverse optical lattice vibrations in quartz. *Phys Rev* 161:903–910.
- Sforna, M.C., Van Zuilen, M.A., and Philippot, P. (2014) Structural characterization by Raman hyperspectral mapping of organic carbon in the 3.46 billion-year-old Apex chert, Western Australia. *Geochim Cosmochim Acta* 124:18–33.
- Steele, A., McCubbin, F.M., Fries, M., Kater, L., Boctor, N.Z., Fogel, M.L., Conrad, P.G., Glamoclija, M., Spencer, M., Morrow, A.L., Hammond, M.R., Zare, R.N., Vicenzi, E.P., Siljeström, S., Bowden, R., Herd, C.D., Mysen, B.O., Shirey, S.B., Amundsen, H.E., Treiman, A.H., Bullock, E.S., and Jull, A.J. (2012) A reduced organic carbon component in martian basalts. *Science* 337:212–215.
- Van Kranendonk, M.J. and Pirajano, F. (2004) Geochemistry of metabasalts and hydrothermal alteration zones associated with c. 3.45 Ga chert and barite deposits: implications for the geological setting of the Warrawoona Group, Pilbara Craton, Australia. *Geochemistry: Exploration, Environment, Analysis* 4:253–278.

Address correspondence to:

D.M. Bower
Planetary Environments Laboratory
NASA Goddard SFC
Greenbelt, MD 20771

E-mail: dina.m.bower@nasa.gov

Submitted 22 July 2014
Accepted 28 October 2015

Abbreviation Used

NHM = Natural History Museum